Energy & Environmental Science

COMMUNICATION

View Article Online
View Journal

Cite this: DOI: 10.1039/c7ee01486d

Received 28th May 2017,
Accepted 10th August 2017

DOI: 10.1039/c7ee01486d

rsc.li/ees

Crystalline nickel manganese antimonate as a stable water-oxidation catalyst in aqueous 1.0 M H_2SO_4†

Ivan A. Moreno-Hernandez,[a] Clara A. MacFarland,[a] Carlos G. Read,[a] Kimberly M. Papadantonakis,[a] Bruce S. Brunschwig[b] and Nathan S. Lewis*[abc]

Water oxidation is a required half-reaction for electrochemical water splitting. To date, the only well-established active oxygen-evolution catalysts stable under operating conditions and at rest in acidic aqueous media contain Ru or Ir, two of the scarcest non-radioactive elements on Earth. We report herein a nickel-manganese antimonate electrocatalyst with a rutile-type crystal structure that requires an initial voltammetric overpotential of 672 ± 9 mV to catalyze the oxidation of water to O_2(g) at a rate corresponding to 10 mA cm^{-2} of current density when operated in contact with 1.0 M sulfuric acid. Under galvanostatic control, the overpotential initially rose from 670 mV but was then stable at 735 ± 10 mV for 168 h of continuous operation at 10 mA cm^{-2}. We additionally provide an in-depth evaluation of the stability of the nickel-manganese antimonate electrocatalyst, including elemental characterization of the surface, bulk, and electrolyte before and after electrochemical operation.

Broader context

Fuel-forming devices that use renewable energy require the oxidation of water in conjunction with a cathodic fuel-forming reaction. The oxygen-evolving catalysts used in acidic electrolytes generally consist of noble metal oxides such as IrO_x and RuO_x, whereas catalysts used in alkaline electrolysis consist of earth-abundant transition metal elements such as Ni and Fe. The difference in catalyst abundance between the two types of systems underscores the difficulty in stabilizing transition metal elements such as Ni and Mn in strongly acidic conditions under anodic current flow. Understanding how to stabilize earth-abundant oxygen-evolving catalysts in acid is important for the development of compact, cost-effective fuel-forming devices that can be scaled to meet global energy demands.

Introduction

Facile conversion of electricity into chemical fuels is an enabling technology for grid-scale energy storage as well as for the production of carbon-neutral transportation fuels.[1] Reductive fuel generation necessitates the oxidation of another molecule. Oxidation of water by the oxygen-evolution reaction (OER) enables release of the oxidized product and the use of atmospheric O_2(g) for oxidation of the fuel. While earth-abundant, low-overpotential electrocatalysts are available for both the hydrogen-evolution and oxygen-evolution reactions in aqueous alkaline media,[2] in acidic electrolytes the only well-established stable OER electrocatalysts are noble metal oxides such as IrO_x and RuO_x.[2–5] The low abundance of Ir and Ru presents challenges for global scalability of associated sustainable energy technologies.[6] Efforts to improve the activity and stability of earth-abundant catalysts for the OER in acid have included searches for acid-stable metal-oxide phases;[7–9] anodic electrodeposition of dissolved transition metals to produce phases that are stable in equilibrium with cations in solution at the OER potential;[10] and doping metal oxides using anions that have high oxidation potentials.[9] Oxides that incorporate two or more metals offer the potential to tune the stability of the material by the formation of new phases that are more stable than the individual metal oxides.[11,12] Synergistic interactions in multimetal electrocatalysts can additionally yield improved activity relative to catalysts formed from the individual metals.[13,14]

According to Pourbaix diagrams, metal oxides of Ni, Mn, and Sb are stable in acidic conditions at OER potentials.[11,12] Furthermore, selected transition-metal antimonates, such as $NiSb_2O_6$, are predicted to be stable at all temperatures with respect to disproportionation to the constituent binary oxides.[15] Thus, Sb was chosen as an element to form ternary or quarternary oxides with Ni and Mn due to the predicted thermodynamic stability under OER conditions in acid and the over 4 orders of magnitude higher annual production of Sb relative to Ir.[6] Accordingly, we report herein the synthesis of solid solutions of crystalline $NiSb_2O_6$ with $MnSb_2O_6$, and report the electrochemical activity

[a] Division of Chemistry and Chemical Engineering, California Institute of Technology, 127-72, Pasadena, CA 91125, USA. E-mail: nslewis@caltech.edu
[b] Beckman Institute Molecular Materials Research Center, California Institute of Technology, Pasadena, CA 91125, USA
[c] Kavli Nanoscience Institute, California Institute of Technology, Pasadena, USA

† Electronic supplementary information (ESI) available. See DOI: 10.1039/c7ee01486d

and stability of the compounds for the OER in acidic media. The electrochemical behavior was characterized over a range of current densities, with emphasis on the performance at 10 mA cm^{-2}, which is characteristic of the operational current density for an ~10% efficient solar fuels device under 1 Sun, nonconcentrated, peak insolation conditions.[2]

Results

$Ni_xMn_{1-x}Sb_{1.6-1.8}O_y$ catalysts were prepared by sputter deposition of the precursor metals onto quartz slides that were coated with a conductive film of antimony-doped tin oxide (ATO).[16] The metal film was annealed in air (details provided in ESI†). For compositions with $x > 0.2$, the $Ni_xMn_{1-x}Sb_{1.6-1.8}O_y$ materials obtained by annealing the films at 700 °C contained rutile-type MSb_2O_6 (Fig. S1, ESI†). The bulk composition of the precursor metal films, shown in Table S1 (ESI†), was measured by inductively coupled plasma mass spectrometry (ICP-MS). Fig. S2 (ESI†) shows the surface composition of the electrocatalysts as determined by X-ray photoelectron spectroscopy (XPS). The atomic ratios of Ni to total transition metals (*i.e.*, Ni/(Ni + Mn)), and of Sb to total transition metals were used to measure their surface segregation. For the as-synthesized material, the ratio of Ni-to-transition metals deduced using XPS (Fig. S2A, ESI†) was similar to the bulk ratio determined using ICP-MS (Table S1, ESI†). However, deviations from the ratio of Sb-to-transition metals of 1.6–1.8 determined from ICP-MS (Table S1, ESI†) indicated that the surface was Sb rich for Mn-rich compositions and was transition-metal rich for Ni-rich compositions (Fig. S2B, ESI†). Antimonates generally exhibit surface enrichment of Sb,[17] however modifications in the synthesis temperature can produce Sb-poor surfaces.[18]

The catalytic activity and stability were evaluated *via* cyclic voltammetry (CV) and chronopotentiometry in 1.0 M H_2SO_4(aq), using methods that closely followed established OER electrocatalyst benchmarking procedures.[2] Fig. 1a shows typical cyclic voltammograms obtained for the family of $Ni_xMn_{1-x}Sb_{1.6-1.8}O_y$ materials when the applied potential was scanned at 10 mV s^{-1} within the range of 1.2 to 2.20 V *versus* a reversible hydrogen electrode (RHE). Fig. 1b summarizes the overpotentials required to produce a current density of 10 mA cm^{-2} (based on the geometric area of the electrodes) for catalysts having the formula $Ni_xMn_{1-x}Sb_{1.6-1.8}O_y$ with a loading of ~0.5 μmol cm^{-2} (Table S1, ESI†). The overpotential, η, for $NiSb_{1.8}O_y$ was 806 ± 9 mV, while $MnSb_{1.7}O_y$ exhibited η = 727 ± 20 mV. Films incorporating both Ni and Mn showed the highest activity (*i.e.* lowest overpotentials) and $Ni_{0.5}Mn_{0.5}Sb_{1.7}O_y$ had the lowest initial overpotential (η = 672 ± 9 mV) of the materials prepared. Resistance compensation had a minimal effect on the measured overpotentials, with all electrodes being corrected less than 15 mV at 10 mA cm^{-2} (Fig. S3A, ESI†). The overpotentials at a current density of 0.1 mA cm^{-2} based on the electrochemically active surface areas of the electrodes (as determined from the double-layer capacitance, see ESI†) indicated that films containing both Ni and Mn showed higher activity than antimonate films containing only Ni or Mn (Fig. S3B, ESI†). The series resistance of $Ni_xMn_{1-x}Sb_{1.6-1.8}O_y$ increased for x = 0.2 and 0.5, indicating a decrease in conductivity of the electrocatalyst film (Fig. S3C, ESI†). The slope in the linear region of the Tafel plot for $NiSb_{1.8}O_y$ was 105 ± 2 mV dec^{-1}, while $MnSb_{1.7}O_y$ exhibited a slope of 96 ± 7 mV dec^{-1} and $Ni_{0.2}Mn_{0.8}Sb_{1.6}O_y$ exhibited the lowest slope measured among the materials, of 60 ± 3 mV dec^{-1}, (Fig. S4A, ESI†). Electrodes made from bare ATO or SbO_y did not exhibit substantial activity for water oxidation in this potential range in 1.0 M H_2SO_4(aq) (Fig. 1a). Faradaic efficiency measurements using electrodes coated with $Ni_{0.5}Mn_{0.5}Sb_{1.7}O_y$ indicated >97% efficiency for O_2(g) production during 60 h of operation (Fig. 1c). The current density at a fixed potential increased with catalyst loading, indicating that increasing the loading of $Ni_{0.5}Mn_{0.5}Sb_{1.7}O_y$ increased the catalytic activity (Fig. S4B, ESI†). The capacitance of the electrode also increased with loading, suggesting that the catalyst film remained permeable to the electrolyte for the film thicknesses studied herein

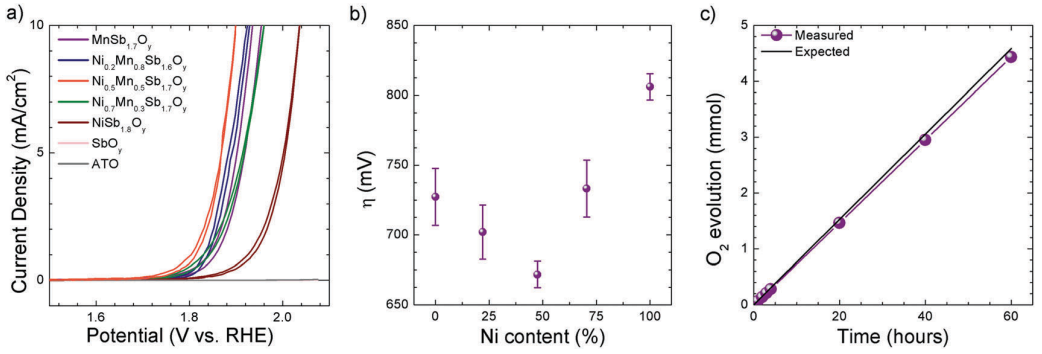

Fig. 1 Electrochemical behavior, activity, and Faradaic efficiency of $Ni_xMn_{1-x}Sb_{1.6-1.8}O_y$ electrodes in 1.0 M H_2SO_4(aq). (a) Cyclic voltammetry at a scan rate of 10 mV s^{-1} of $Ni_xMn_{1-x}Sb_{1.6-1.8}O_y$, SbO_y, and ATO electrodes. (b) Average overpotential at 10 mA cm^{-2} determined from cyclic voltammetry data at a scan rate of 10 mV s^{-1} for $Ni_xMn_{1-x}Sb_{1.6-1.8}O_y$. Ni content defined as percent of transition metals in the as-synthesized film. The overpotentials for $NiSb_{1.8}O_y$, $MnSb_{1.7}O_y$, and $Ni_{0.5}Mn_{0.5}Sb_{1.7}O_y$ were 806 ± 9 mV, 727 ± 20 mV, and 672 ± 9 mV, respectively. The error bars indicate one standard deviation from at least 3 samples. (c) Faradaic efficiency measurements performed with an eudiometer while a $Ni_{0.5}Mn_{0.5}Sb_{1.7}O_y$ electrode was maintained galvanostatically at 10 mA cm^{-2}. The average Faradaic efficiency was 93% from 0 to 4 h and 97% from 20 to 60 h.

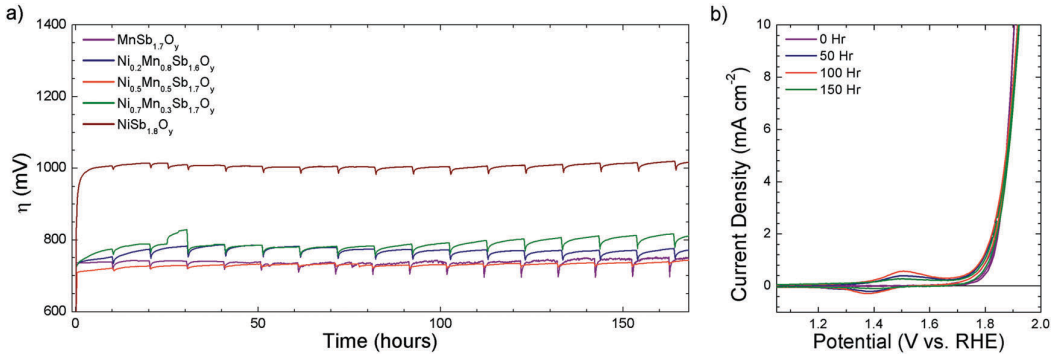

Fig. 2 Chronopotentiometric stability of $Ni_xMn_{1-x}Sb_{1.6-1.8}O_y$ electrodes. (a) Chronopotentiometry at 10 mA cm^{-2} of the $Ni_xMn_{1-x}Sb_{1.6-1.8}O_y$ family in 1.0 M H_2SO_4(aq). (b) Cyclic voltammetry at 10 mV s^{-1} of $Ni_{0.5}Mn_{0.5}Sb_{1.7}O_y$ in between chronopotentiometry.

(Fig. S4C, ESI†). The initial turnover frequency at 0.65 V *vs.* RHE was 0.03 s^{-1} based on the loading of the catalyst and was 0.67 s^{-1} based on the surface area determined by the measured differential capacitance.

Fig. 2a shows chronopotentiometric stability data for the $Ni_xMn_{1-x}Sb_{1.6-1.8}O_y$ family during galvanostatic control at 10 mA cm^{-2}. A transient decrease in the overpotential was observed when cyclic voltammograms were collected, as well as when the experiment was paused every 1–3 days to replenish the electrolyte. No substantial loss of activity was observed after placing the electrodes in fresh electrolyte. $Ni_{0.7}Mn_{0.3}Sb_{1.7}O_y$ showed an increase in overpotential from 25–30 h due to the electrode being partially blocked by a bubble after electrolyte replenishment. For all of the materials, the overpotentials at 10 mA cm^{-2} varied over the course of the test by less than 5% from the average value for that electrode. The overpotential for $Ni_{0.5}Mn_{0.5}Sb_{1.7}O_y$ initially increased from ~672 mV to ~735 mV but then remained at 735 ± 10 mV for 168 h. Based on the 168 h of continuous operation at 10 mA cm^{-2}, the turnover number of $Ni_{0.5}Mn_{0.5}Sb_{1.7}O_y$ exceeded 33 000 (by loading) and 120 000 (by capacitance). Holding $Ni_{0.5}Mn_{0.5}Sb_{1.7}O_y$ at open circuit for 16 h had little effect on the overpotential (Fig. S5, ESI†), demonstrating that the stability of $Ni_{0.5}Mn_{0.5}Sb_{1.7}O_y$ does not depend upon application of a potential positive of the thermodynamic potential required for water oxidation. Cyclic voltammetry measurements performed at intervals during chronopotentiometry on $Ni_{0.5}Mn_{0.5}Sb_{1.7}O_y$ electrodes exhibited the development of redox peaks centered at 1.46 V *versus* RHE (Fig. 2b). The development of similar redox peaks was observed for $MnSb_{1.7}O_y$ samples, but not for $NiSb_{1.8}O_y$ (Fig. S6A, ESI†). $Ni_{0.5}Mn_{0.5}O_y$ electrodes without Sb, as well as ATO and SbO_y electrodes exhibited $\eta > 1300$ mV after <10 min at 10 mA cm^{-2} (Fig. S6B, ESI†), consistent with previous reports of the OER behavior of NiO_y and MnO_y in 1 M acid.[2]

ICP-MS was used to determine the concentration of dissolved metals in the electrolyte at different times during the chronopotentiometric stability test (details provided in ESI†). Approximately 56, 17, and 11 percent of the Mn, Ni, and Sb, respectively, from a $Ni_{0.5}Mn_{0.5}Sb_{1.7}O_y$ electrode had leached into the electrolyte after 144 h at 10 mA cm^{-2} (Fig. S7, ESI†). For all elements measured, the leach rate decreased with time and after 120 h was zero within the error of the ICP-MS technique. The capacitance of the electrode also increased during chronopotentiometry at 10 mA cm^{-2} (Fig. S6C, ESI†), which is consistent with increased porosity arising from the dissolution of electrode material during electrolysis.

Fig. 3 compares high-resolution transmission-electron microscope images (HRTEM) of the surface of $Ni_{0.5}Mn_{0.5}Sb_{1.7}O_y$ before and after operation for 144 h at 10 mA cm^{-2} in 1.0 M H_2SO_4(aq). The observed lattice spacing of ~3.3 Å closely matches the (110) planes of the rutile-type MSb_2O_6,[19] and is consistent with X-ray diffraction data collected after electrochemical operation (Fig. S8, ESI†). The HRTEM images showed no crystalline or amorphous impurities at the surface of the as-synthesized electrodes. High-angle annular dark-field (HAADF) images did not show substantial changes in the ~300 nm thickness of an electrocatalyst film (corresponding to a catalyst loading of 0.48 μmol cm^{-2}) after operation for 144 h (Fig. S9, ESI†). Scanning-electron microscopy (SEM) images of $Ni_{0.5}Mn_{0.5}Sb_{1.7}O_y$-coated electrodes before and after electrochemical operation were consistent with the presence of polycrystalline surfaces (Fig. S10, ESI†). The STEM-EDS spectrum of the as-synthesized $Ni_{0.5}Mn_{0.5}Sb_{1.7}O_y$ film further confirmed the presence of Ni, Mn, and Sb, with no other

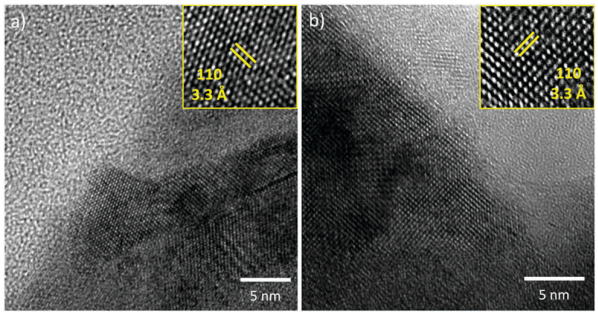

Fig. 3 Structural characterization of $Ni_{0.5}Mn_{0.5}Sb_{1.7}O_y$ electrocatalyst. Transmission-electron microscopy of $Ni_{0.5}Mn_{0.5}Sb_{1.7}O_y$ (a) before and (b) after chronopotentiometry for 144 h at 10 mA cm^{-2} of geometric area, highlighting the 3.3 Å lattice fringes that correspond to the (110) planes. The dark areas represent the catalyst and the dark/light interface is the part of the samples that was in contact with the electrolyte.

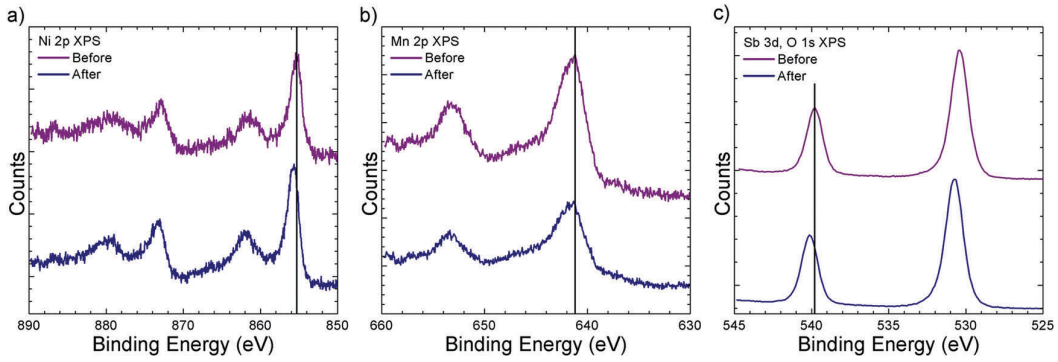

Fig. 4 Chemical characterization of $Ni_{0.5}Mn_{0.5}Sb_{1.7}O_y$ electrocatalyst. High-resolution XPS data of $Ni_{0.5}Mn_{0.5}Sb_{1.7}O_y$ before and after chronopotentiometry for 144 h at 10 mA cm^{-2}. The spectral regions are: (a) Ni 2p, (b) Mn 2p, (c) Sb 3d and O 1s. The spectra were normalized so that the integrated signals of the Ni 2p, Mn 2p, and Sb 3d peaks were the same for both samples.

observable impurities (Fig. S11, ESI†). No Ir or Ru was detectable by high-resolution XPS after electrochemical operation of the catalyst film (Fig. S12, ESI†).

Fig. 4 presents high-resolution Mn 2p, Ni 2p, and Sb 3d XPS data for a $Ni_{0.5}Mn_{0.5}Sb_{1.7}O_y$-coated electrode before and after electrochemical operation, respectively. After electrolysis, the Ni 2p and Sb 3d peaks shifted towards higher binding energies by 0.39 ± 0.10 eV and 0.33 ± 0.09 eV, respectively. The surface composition determined *via* XPS for $Ni_{0.5}Mn_{0.5}Sb_{1.7}O_y$ was 1 : 0.98 : 4.15 ± 0.05 Ni : Mn : Sb before electrochemical operation and was 1 : 0.48 : 3.67 ± 0.03 Ni : Mn : Sb after electrochemical operation. The surface composition determined *via* XPS for $Ni_{0.7}Mn_{0.3}Sb_{1.7}O_y$ was 1 : 0.50 ± 0.16 Ni : Mn and 1 : 2.98 ± 0.93 Ni : Sb after electrochemical operation. The bulk composition determined by EDS for $Ni_{0.5}Mn_{0.5}Sb_{1.7}O_y$ was 1 : 1.10 : 3.57 ± 0.03 Ni : Mn : Sb before electrochemical operation and was 1 : 1.03 : 4.44 ± 0.03 Ni : Mn : Sb after electrochemical operation.

Fig. S13 (ESI†) shows the effect of the annealing temperature on the electrochemical stability of $Ni_{0.5}Mn_{0.5}Sb_{1.7}O_y$. For films annealed at 500 °C, the overpotential increased to $\eta > 1000$ mV in <1 min, whereas films annealed at 700 °C exhibited $\eta \sim 745$ mV for 168 h (Fig. S13 (ESI†) and Fig. 1b). XRD of these films indicated that the MSb_2O_6 phase formed at and above 700 °C but not at 500 °C (Fig. S14, ESI†). $NiSb_2O_y$ and $MnSb_2O_y$ undergo a transformation from amorphous to crystalline material at ~ 615 °C and ~715 °C, respectively.[20] Films annealed at 900 °C could not be evaluated, due to their high resistance (>10 kΩ) as determined from impedance measurements of the resulting electrodes, compared to the resistance exhibited by films annealed at 700 °C (<150 Ω). The ATO sheet resistance as determined by four-point probe measurements changed little with temperature, and was 17.2 ± 0.9 Ω sq^{-1} for the as-prepared films, 17.2 ± 1.0 Ω sq^{-1} for films annealed at 700 °C, and 21.4 ± 1.0 Ω sq^{-1} for films that had been annealed at 900 °C.

Discussion

The activity of the $Ni_xMn_{1-x}Sb_{1.6-1.8}O_y$ family of electrocatalysts was highest when both Ni and Mn were initially present at equal concentrations in the film. The enhanced activity is not primarily due to changes in film resistance because a higher resistance was observed for x = 0.2 and 0.5 (~100 Ω) electrodes compared to x = 0, 0.7, 1 (<50 Ω) electrodes (Fig. S3C, ESI†). Synergistic interactions have been observed for other water-oxidation catalysts, such as $Ni_{1-x}Fe_xOOH$ in alkaline media.[21] The rutile crystal phase appears to favorably affect the electrochemical stability of $Ni_xMn_{1-x}Sb_{1.6-1.8}O_y$ materials for use as oxygen-evolving electrocatalysts in strongly acidic electrolytes. The formation of $NiSb_2O_6$ from NiO and Sb_2O_5 is more favorable than decomposition of $NiSb_2O_6$ to Sb_2O_5 accompanied by subsequent dissolution of NiO to produce Ni^{2+} in pH 0 solution.[15,22] Hence, the dissolution of Ni is inhibited by the formation of the more stable Ni-containing antimonate phase. Together these results suggest a strategy for discovery of acid-stable water-oxidation catalysts through identification of thermodynamically stable crystalline ternary oxides followed by tuning the electrocatalytic activity and stability of the oxides by altering the ratio between the transition metals in the oxides.

Preferential leaching of Mn from the $Ni_{0.5}Mn_{0.5}Sb_{1.7}O_y$ material is evidenced by Mn detected by ICP-MS in the electrolyte after electrolysis, resulting in the surface enrichment of Ni observed by XPS. Surface enrichment of Sb increases with an increase of Mn in the film, which may be due to poor crystallization kinetics of $MnSb_2O_6$ at 700 °C. Other OER electrocatalysts, such as $SrIrO_3$ and $Fe_1Co_{1.02}W_{0.7}$ oxyhydroxides, also leach initially under operation, thereby forming a more stable catalyst.[5,13] The leaching of Mn from a $Ni_xMn_{1-x}Sb_{1.6-1.8}O_y$ structure with $x > 0.5$ could produce a film that does not have the same surface structure as one obtained directly by annealing metal films of the same final composition. Formation of amorphous, active phases throughout the catalyst film cannot be excluded. Alternatively, the leaching of Mn could be due to the dissolution of materials that did not form a ternary rutile-type oxide with Sb, thus exposing the stable crystalline phase. The capacitance increased by a factor of ~6 after electrochemical operation (Fig. S6C, ESI†), with minimal changes in thickness (Fig. S9, ESI†), indicating an increase in porosity of the catalyst film.

The Ni 2p, Mn 2p, and Sb 3d spectra both indicated that before electrochemical operation Ni, Mn, and Sb were in 2+, 2+ and 3+ oxidation states, respectively, at the surface (Table S2, see ESI†).[23,24] The shift of the peaks in the XPS data suggest that the surface oxidation states for small amounts of Ni and large amounts of Sb increase during electrochemical operation. The Ni and Sb signals exhibited a shift towards higher binding energies by 0.39 and 0.33 eV, respectively. Before electrochemistry, the XPS data in the Ni 2p and Mn 2p regions closely resembled spectra reported for Ni^{2+} and Mn^{2+} (Table S2, ESI†).[23] The $\sim$1 eV shift of the XPS Ni $2p_{3/2}$ maximum between NiO and NiOOH suggests that Ni is partially oxidized.[23] The surfaces of transition metal antimonates usually consist of a mixture of Sb^{3+} and Sb^{5+}. The observed 0.33 eV shift of the Sb $3d_{3/2}$ peak suggests that after electrochemistry the surface Sb was oxidized, indicating that the surface changed from having a substantial Sb^{3+} component to adopting more Sb^{5+} character, which could be due to the removal of an Sb-rich surface layer that did not form a rutile-type structure. The Sb^{5+} component is consistent with the rutile-type bulk structure. The increase in the oxidation state of surficial Sb and the small initial loss of Sb during electrolysis as measured by ICP-MS (Fig. S7, ESI†) suggest that the surface was initially partially covered by oxides that did not form a rutile-type structure and dissolved over time. The ability of transition metals to accept various oxidation states within a material is often required in proposed mechanisms of the oxygen-evolution reaction.[25]

The most active OER catalysts in acidic electrolytes, such as $IrO_x/SrIrO_3$, exhibit η = 270–290 mV at 10 mA cm^{-2} of current density.[5] Molecular oxygen-evolving catalysts based on Ru and other precious metals exhibit turnover numbers of $<$43 000 in acidic media, and their stability is limited to a few hours.[26,27] Electrodeposited Fe–Ni oxyhydroxide exhibits η = 286–340 mV in 1.0 M KOH(aq),[2,28] whereas deposition of Fe–Ni oxyhydroxide by pulsed-laser ablation yields η = 280 mV at these same geometric electrode current densities.[29] Co oxide prepared in phosphate- or borate-buffered aqueous solutions exhibits η = 390–410 mV at 10 mA cm^{-2},[30] and is unstable after 10 min of water oxidation at current densities of 10 mA cm^{-2} in pH $<$ 12 electrolytes.[31] CoFe Prussian blue compounds exhibit η $<$ 820 mV at 10 mA cm^{-2} for 2 h in pH 2.2 electrolyte.[32] MnO_y exhibits η $\sim$ 500 mV at 2 μA cm^{-2} in pH 1 electrolyte, with a projected η = 1.96 V at 10 mA cm^{-2} based on the reported Tafel slope, and has a turnover number for water oxidation of $<$1 and is unstable at open circuit.[3] $Ni_{0.5}Mn_{0.5}Sb_{1.7}O_y$ exhibits η $\sim$ 745 mV at 10 mA cm^{-2} in pH 0 electrolyte with a turnover number $>$33 000.

Although the overpotentials of the reported $Ni_xMn_{1-x}Sb_{1.6-1.8}O_y$ family are 300–450 mV higher than state-of-the-art catalysts, their stability is comparable to the noble metal oxides, which are known to corrode under operation.[4,33] Crystalline antimonates have not been thoroughly optimized or explored for water oxidation. For the $Ni_xMn_{1-x}Sb_2O_6$ family, further improvements could be made by optimizing the synthesis method to improve the conductivity of the catalyst, incorporate more Mn without dissolution, aid in the identification of actives sites of the catalyst, and increase the density of catalytically active sites. Furthermore, many other earth-abundant transition metals form rutile-type oxides with antimony, and their stability and activity towards water oxidation in acid is unknown. Further studies on the activity and stability of the transition metal antimonates, along with a mechanistic understanding of the electrocatalyst enhancement, could thus potentially lead to development of earth-abundant catalysts with activities comparable to noble metal oxides.

The long-term activity of $Ni_{0.5}Mn_{0.5}Sb_{1.7}O_y$ is sufficient to construct an electrolyzer that is 57% efficient (see ESI†). Electrolyzers and integrated solar-fuels devices that use strongly acidic or alkaline media allow for the efficient evolution of $H_2(g)$ and $O_2(g)$ in intrinsically safe systems, while also producing $H_2(g)$ under pressure to facilitate beneficial separation and collection of the evolved gases.[34] The 745 mV OER overpotential is also sufficient to construct solar-fuels devices that have energy-conversion efficiencies of $>$20%, in conjunction with optimized, compatible, acid-stable light absorbers and membranes.[35] Further improvements in OER performance will require development of more active, stable, non-precious metal electrocatalysts for water oxidation, perhaps building upon the ternary metal oxide approach to obtain stability and OER activity in oxidizing aqueous acidic media.

Conclusion

$Ni_xMn_{1-x}Sb_{1.6-1.8}O_y$ acts as a stable water-oxidation electrocatalyst for $>$168 h of continuous operation in aqueous 1.0 M sulfuric acid. The stability of the electrocatalyst was related to the formation of a crystalline MSb_2O_6 rutile-type phase. The activity was optimized when both Ni and Mn were present in approximately equal amounts. Anodic exposure in 1.0 M H_2SO_4(aq) resulted in preferential leaching of Mn and oxidation of the surface Ni and Sb. The observations suggest an approach towards further development of crystalline ternary or quaternary oxides consisting of earth-abundant elements for water oxidation in aqueous acidic media.

Conflicts of interest

There are no conflicts to declare.

Acknowledgements

This work is supported through the Office of Science of the U.S. Department of Energy (DOE) under award no. DE-SC0004993 to the Joint Center for Artificial Photosynthesis, a DOE Energy Innovation Hub. I. M. H. acknowledges a National Science Foundation Graduate Research Fellowship under Grant No. DGE-1144469. This work was also supported by the Gordon and Betty Moore Foundation under Award No. GBMF1225. C. G. R. acknowledges the Resnick Sustainability Institute for a post-doctoral fellowship. We thank N. Dalleska and P. Buabthong for assistance with mass spectroscopy measurements and X-ray photoelectron spectroscopy measurements, respectively.

References

1 N. S. Lewis, *Science*, 2016, **351**, aad1920.
2 C. C. McCrory, S. Jung, I. M. Ferrer, S. M. Chatman, J. C. Peters and T. F. Jaramillo, *J. Am. Chem. Soc.*, 2015, **137**, 4347–4357.
3 M. Huynh, D. K. Bediako and D. G. Nocera, *J. Am. Chem. Soc.*, 2014, **136**, 6002–6010.
4 N. Danilovic, R. Subbaraman, K. C. Chang, S. H. Chang, Y. J. Kang, J. Snyder, A. P. Paulikas, D. Strmcnik, Y. T. Kim, D. Myers, V. R. Stamenkovic and N. M. Markovic, *J. Phys. Chem. Lett.*, 2014, **5**, 2474–2478.
5 L. C. Seitz, C. F. Dickens, K. Nishio, Y. Hikita, J. Montoya, A. Doyle, C. Kirk, A. Vojvodic, H. Y. Hwang, J. K. Norskov and T. F. Jaramillo, *Science*, 2016, **353**, 1011–1014.
6 P. C. K. Vesborg and T. F. Jaramillo, *RSC Adv.*, 2012, **2**, 7933.
7 R. Frydendal, E. A. Paoli, I. Chorkendorff, J. Rossmeisl and I. E. L. Stephens, *Adv. Energy Mater.*, 2015, **5**, 1500991.
8 A. Shinde, R. J. R. Jones, D. Guevarra, S. Mitrovic, N. Becerra-Stasiewicz, J. A. Haber, J. Jin and J. M. Gregoire, *Electrocatalysis*, 2014, **6**, 229–236.
9 P. P. Patel, M. K. Datta, O. I. Velikokhatnyi, R. Kuruba, K. Damodaran, P. Jampani, B. Gattu, P. M. Shanthi, S. S. Damle and P. N. Kumta, *Sci. Rep.*, 2016, **6**, 28367.
10 L. G. Bloor, P. I. Molina, M. D. Symes and L. Cronin, *J. Am. Chem. Soc.*, 2014, **136**, 3304–3311.
11 A. Jain, S. P. Ong, G. Hautier, W. Chen, W. D. Richards, S. Dacek, S. Cholia, D. Gunter, D. Skinner, G. Ceder and K. A. Persson, *APL Mater.*, 2013, **1**, 011002.
12 A. Jain, G. Hautier, S. P. Ong, C. J. Moore, C. C. Fischer, K. A. Persson and G. Ceder, *Phys. Rev. B: Condens. Matter Mater. Phys.*, 2011, **84**, 045115.
13 B. Zhang, X. Zheng, O. Voznyy, R. Comin, M. Bajdich, M. García-Melchor, L. Han, J. Xu, M. Liu, L. Zheng, F. P. García de Arquer, C. T. Dinh, F. Fan, M. Yuan, E. Yassitepe, N. Chen, T. Regier, P. Liu, Y. Li, P. De Luna, A. Janmohamed, H. L. Xin, H. Yang, A. Vojvodic and E. H. Sargent, *Science*, 2016, **352**, 333–337.
14 R. D. L. Smith, M. S. Prévot, R. D. Fagan, Z. Zhang, P. A. Sedach, M. K. J. Siu, S. Trudel and C. P. Berlinguette, *Science*, 2013, **340**, 60–63.
15 K. Swaminathan and O. M. Sreedharan, *J. Alloys Compd.*, 1999, **292**, 100–106.
16 H. Bisht, H.-T. Eun, A. Mehrtens and M. A. Aegerter, *Thin Solid Films*, 1999, **351**, 109–114.
17 G. I. Straguzzi, K. B. Bischoff, T. A. Koch and G. C. A. Schuit, *J. Catal.*, 1987, **103**, 357–365.
18 N. Burriesci, F. Garbassi, M. Petrera and G. Petrini, *J. Chem. Soc., Faraday Trans. 1*, 1982, **78**, 817–833.
19 J. N. Reimers, J. E. Greedan, C. V. Stager and R. Kremer, *J. Solid State Chem.*, 1989, **83**, 20–30.
20 G. Westin and M. Nygren, *J. Mater. Chem.*, 1993, **3**, 367–371.
21 D. Friebel, M. W. Louie, M. Bajdich, K. E. Sanwald, Y. Cai, A. M. Wise, M. J. Cheng, D. Sokaras, T. C. Weng, R. Alonso-Mori, R. C. Davis, J. R. Bargar, J. K. Norskov, A. Nilsson and A. T. Bell, *J. Am. Chem. Soc.*, 2015, **137**, 1305–1313.
22 B. Beverskog and I. Puigdomenech, *Corros. Sci.*, 1997, **39**, 969–980.
23 M. C. Biesinger, B. P. Payne, A. P. Grosvenor, L. W. M. Lau, A. R. Gerson and R. S. C. Smart, *Appl. Surf. Sci.*, 2011, **257**, 2717–2730.
24 R. Delobel, H. Baussart, J.-M. Leroy, J. Grimblot and L. Gengembre, *J. Chem. Soc., Faraday Trans. 1*, 1983, **79**, 879–891.
25 T. Reier, H. N. Nong, D. Teschner, R. Schlögl and P. Strasser, *Adv. Energy Mater.*, 2016, 1601275, DOI: 10.1002/aenm.201601275.
26 Y. Jiang, F. Li, B. Zhang, X. Li, X. Wang, F. Huang and L. Sun, *Angew. Chem., Int. Ed.*, 2013, **52**, 3398–3401.
27 M. D. Karkas, O. Verho, E. V. Johnston and B. Akermark, *Chem. Rev.*, 2014, **114**, 11863–12001.
28 K. Sun, I. A. Moreno-Hernandez, W. C. Schmidt, X. Zhou, J. C. Crompton, R. Liu, F. H. Saadi, Y. Chen, K. M. Papadantonakis and N. Lewis, *Energy Environ. Sci.*, 2017, **10**, 987–1002.
29 B. M. Hunter, J. D. Blakemore, M. Deimund, H. B. Gray, J. R. Winkler and A. M. Muller, *J. Am. Chem. Soc.*, 2014, **136**, 13118–13121.
30 Y. Surendranath, M. Dinca and D. G. Nocera, *J. Am. Chem. Soc.*, 2009, **131**, 2615–2620.
31 A. Minguzzi, F.-R. F. Fan, A. Vertova, S. Rondinini and A. J. Bard, *Chem. Sci.*, 2012, **3**, 217–229.
32 L. Han, P. Tang, A. Reyes-Carmona, B. Rodriguez-Garcia, M. Torrens, J. R. Morante, J. Arbiol and J. R. Galan-Mascaros, *J. Am. Chem. Soc.*, 2016, **138**, 16037–16045.
33 S. Cherevko, A. R. Zeradjanin, A. A. Topalov, N. Kulyk, I. Katsounaros and K. J. J. Mayrhofer, *ChemCatChem*, 2014, **6**, 2219–2223.
34 C. Xiang, K. M. Papadantonakis and N. S. Lewis, *Mater. Horiz.*, 2016, **3**, 169–173.
35 Y. Chen, S. Hu, C. Xiang and N. S. Lewis, *Energy Environ. Sci.*, 2015, **8**, 876–886.

